Structural and magnetic properties of the Kagomé antiferromagnet YbBaCo$_4$O$_7$

A. Huq[a], J.F. Mitchell[b],*, H. Zheng[b], L.C. Chapon[c], P.G. Radaelli[c],
K.S. Knight[c], P.W. Stephens[d]

[a]*Intense Pulsed Neutron Source, Argonne National Laboratory, 9700 S. Cass Ave., Argonne, IL 60439, USA*
[b]*Materials Science Division, Argonne National Laboratory, 9700 S. Cass Ave., Argonne, IL 60439, USA*
[c]*ISIS Facility, Rutherford Appleton Laboratory-CCLRC, Chilton, Didcot, Oxfordshire, OX11 0QX, UK*
[d]*Department of Physics and Astronomy, SUNY Stonybrook, NY 11794, USA*

Abstract

The mixed-valent compound YbBaCo$_4$O$_7$ is built up of Kagomé sheets of CoO$_4$ tetrahedra, linked in the third dimension by a triangular layer of CoO$_4$ tetrahedra in an analogous fashion to that found in the known geometrically frustrated magnets such as pyrochlores and SrCr$_{9x}$Ga$_{12-9x}$O$_{19}$ (SCGO). We have undertaken a study of the structural and magnetic properties of this compound using combined high-resolution powder neutron and synchrotron X-ray diffraction. YbBaCo$_4$O$_7$ undergoes a first-order trigonal→ orthorhombic phase transition at 175 K. We show that this transition occurs as a response to a markedly underbonded Ba^{2+} site in the high-temperature phase and does not appear to involve charge ordering of Co^{2+}/Co^{3+} ions in the tetrahedra. The symmetry lowering relieves the geometric frustration of the structure, and a long-range-ordered 3-D antiferromagnetic state develops below 80 K.
© 2006 Published by Elsevier Inc.

Keywords: Geometric frustration; Cobaltite; Charge-order; Neutron diffraction; Kagomé; Mixed-valent

1. Introduction

Transition metal oxides (TMO) offer a wealth of opportunities to study exotic electronic and magnetic states, as evidenced by colossal magnetoresistance in manganites, spin-state transitions in cobaltites, and orbital liquid states in vanadates and titanates. An area in which TMO have been particularly valuable is the field of geometrically frustrated magnets, where oxide spinels, pyrochlores, ladder-compounds, etc., enable one to explore how the global system—spin, charge, lattice—responds to the constraints of structure-enforced frustration. One structural motif commonly associated with geometric frustration is that of the Kagomé net, found in a variety of compounds such as pyrochlores, jarosites, etc. [1–3]. A specific example of a Kagomé net containing compound that has received substantial attention is SrCr$_{9x}$Ga$_{12-9x}$O$_{19}$

(SCGO) [2,4–8]. SCGO is actually built up of double Kagomé sheets of Cr^{3+} with a triangular layer of Cr^{3+} sandwiched between the sheets and linking them to form Cr^{3+} tetrahedra. The double Kagomé sheet is capped on both sides by Ga^{3+} ions, effectively isolating it from neighboring layers. The result is a frustrated $S = 3/2$ antiferromagnet with a frustration index $T_s/|\theta_W| \sim 120$ [6], where T_s is a spin-glass transition temperature, and θ_W is the Weiss temperature.

Recently, a ternary cobalt compound with formula RBaCo$_4$O$_7$ (hereafter referred to as R-114) has been reported, with R = Y, Tb, Dy, Ho, Er, Tm, Yb, Lu [9–14]. This compound, isostructural with LuBaZn$_3$AlO$_7$ [15], is shown in Fig. 1, and possesses a 3:1 ratio of Co^{2+} to Co^{3+}, which creates the potential for real-space charge order over the two crystallographically distinct Co sites. The crystal structure is built up of Kagomé sheets of CoO$_4$ tetrahedra, linked by triangular layers of CoO$_4$ tetrahedra in much the same way as SCGO. Indeed, considering two Kagomé sheets and their linking and capping tetrahedra,

*Corresponding author. Fax: +630 252 7777.
E-mail address:* mitchell@anl.gov (J.F. Mitchell).
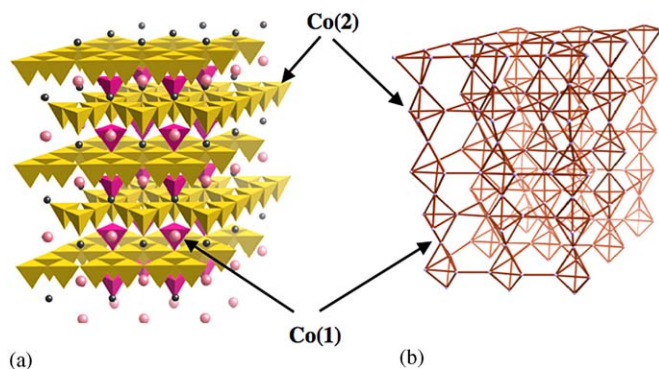
Fig. 1. (a) Crystal structure of YbBaCo$_4$O$_7$ at 225 K in space group $P31c$. Ba^{2+} ions are represented by large white spheres, while Yb^{3+} are represented by small, dark spheres. (b) Co network of YbBaCo$_4$O$_7$ at 225 K.

R-114 differs from the double Kagomé sheet motif found in SCGO by the substitution of a magnetic Co ion for nonmagnetic Ga^{3+}. The presence of this magnetic ion makes the Co sublattice structure of *R*-114 analogous to that found in the 3-D geometrically frustrated pyrochlore lattice. The difference is that the triangular layers found in the pyrochlore lattice are stacked […ABCABC…] along [111] of the cubic lattice, while in *R*-114 these layers stack […AAA…] along the hexagonal [001]. The latter stacking sequence generates the chains of face-sharing tetrahedra highlighted in Fig. 1b. The structural similarities of *R*-114 to SCGO and to pyrochlores makes the system a potential new addition to the family of geometrically frustrated magnets.

A few studies of the Y-114 member (and substituted analogs) have recently appeared [9–14]. Neutron diffraction and magnetic studies on Y-114 by Valldor and Andersson [14] have shown that this compound is not geometrically frustrated but rather antiferromagnetically ordered with a ferromagnetic component or perhaps a spin-glass state at low temperature. Likewise, Tsipis et al. [10] propose a spin-glass state for Y-114. Bychkov et al. [9] have flux-grown small crystals of Tb-114 compounds, but reported no structural or magnetic characterization. An X-ray diffraction study on a single crystal of Y-114 by Valldor and Andersson [14] revealed no clear evidence of charge order at room temperature based on bond-valence sum calculations, but based on size arguments it was suggested that the triangular layer of tetrahedra should be preferentially Co^{3+}. Temperature-dependent studies by this group showed no evidence of symmetry lowering for the Y-114 system that might accompany charge-order, but no data have been reported on the other analogs in the *R*-114 family.

In this paper, we report a full crystallographic characterization of the YbBaCo$_4$O$_7$ phase in the range $1.7\,\text{K} \leqslant T \leqslant 225\,\text{K}$. In particular, we detail a first-order structural phase transition at 175 K that reduces the symmetry from trigonal (space group $P31c$) to orthorhombic (space group $Pbn2_1$) with an $(a, \sqrt{3}a, c)$ supercell. This

symmetry lowering is driven by an extremely underbonded Ba^{2+} ion, for which the Ba–O coordination number increases dramatically to satisfy its bond-valence requirements. A consequence of this structural instability is a symmetry lowering that lifts the geometric frustration, enabling the system to order at ~80 K into a long-range 3-D antiferromagnet. Additionally, magnetic measurements demonstrate that the AFM state is unstable to moderate applied magnetic fields, which stabilize a ferromagnetic component.

2. Experimental

Samples of YbBaCo$_4$O$_{7+\delta}$ (Yb-114) were prepared by a standard ceramic technique, with a final firing at 1150 °C in air followed by furnace cooling. The as-made sample was treated in a nitrogen atmosphere to obtain a sample with $\delta = -0.05(5)$ as determined by reduction in a 5% H$_2$/Ar mixture on a Perkin-Elmer TGA-7. Powder neutron diffraction data were collected at 225 and 150 K on the High-Resolution Powder Diffractometer at the ISIS facility of the Rutherford Appleton Laboratory. A 1.8 g sample was loaded into a flat plate container with 0.2 mm vanadium windows. Time-of-flight diffraction patterns obtained from two detector banks located at 168° and 90°, respectively, were analyzed simultaneously. Additional data sets were also collected at 90 and 1.7 K on the GEM diffractometer, to access magnetic scattering at low-Q with better statistics. High-resolution X-ray powder diffraction data were collected on beamline X-3B1 at the National Synchrotron Light Source. X-rays of wavelength 0.6989 Å were selected by a Si(111) double-crystal monochromator. Samples were mounted on a flat brass plate, and data were collected in the reflection geometry at 225 and 150 K for the nitrogen-treated sample. The diffracted X-rays were selected by a Ge(111) analyzer crystal on the detector arm to obtain angular resolution of ~0.01°. X-ray data were also collected for the as-made sample at room temperature and 100 K using X-rays of wavelength 0.6567 Å. In order to determine the transition temperature for the structural phase transition data were collected over a short range $(27.4 < 2\Theta < 27.8)$ from 98 to 226 K at 5 K intervals. A short dataset was also collected at 10 K to confirm no further structural changes at low temperature. Full-pattern Rietveld analysis of the neutron and X-ray data was accomplished using Fullprof [16] and GSAS [17], respectively. For joint refinements, X-ray and neutron data were equally weighted. Magnetic and transport data were measured on a Quantum Design Physical Properties Measurement instrument, locally modified for DC transport measurements.

3. Results and discussion

Samples of Yb-114 as prepared in air are oxygen hyperstoichiometric. TGA analysis by reduction in a dilute hydrogen atmosphere indicates that the oxygen content of

our as-prepared sample is 7.19(3) oxygen per formula unit. The excess oxygen is consistent with recent reports from Tsipis et al. [10] of $YBaCo_4O_{7+\delta}$ prepared with δ as large as 1.5. Below we show using synchrotron X-ray data that the as-prepared sample is actually biphasic, containing two Yb-114 phases with slightly different lattice constants. Treatment at 900 °C in nitrogen removes the excess oxygen, with a resultant 6.95(5) oxygen content as determined by TGA. This oxygen-stoichiometric single-phase sample is the subject of the studies reported herein.

Fig. 2a shows DC magnetization as a function of temperature measured on warming in a 1 T applied field after either zero-field cooling (ZFC) or field cooling (FC) in 1 T. The ZFC data are dominated by a paramagnetic response from the Yb^{3+} ions ($J = 7/2$), but superimposed on this background are two features at $T = 80$ and $175\,K$. The former correlates with a transition into a long-range ordered antiferromagnetic state, as shown by powder neutron diffraction (vide infra). The anomaly at $175\,K$ is not a magnetic transition, but rather is a magnetic response to a structural phase transition. Presumably the detailed magnetic exchange constants among Co and/or Yb ions is discontinuously modified as a result of this structural rearrangement. The inset of Fig. 2a shows that this feature appears with hysteresis, indicating its first-order nature. Electrical transport measurements (not shown) also exhibit a signature of this anomaly, with the resistivity jumping by an order of magnitude across the transition with thermal hysteresis. The FC curve is dramatically different than the ZFC data. At 80 K, the magnetization abruptly increases, and a field-induced state appears.

Additional insight into this high-field state is revealed through isothermal magnetization measurements, such as that shown at 25 K in Fig. 2b. In this case, the sample was ZFC to the measuring temperature, and $M(H)$ measured. At 25 K, for fields $H_c < 2.5\,T$, $M(H)$ is linear and reversible, characteristic of the presumed AFM state. However, if the field is increased beyond $H_c(25\,K) = 2.5\,T$, a change in

slope is observed. This transition is irreversible—reducing the field after exceeding H_c results in the sample entering a field-induced state that persists through additional magnetic field cycling. Heating the sample to temperatures well above 80 K followed by ZFC returns it to the AFM state. As shown in the inset to Fig. 2b, H_c is found to be a strong function of temperature, varying from 7.5 T at 2 K to 0.05 T at 75 K. We note that isothermal magnetization measurements on an Y-114 analog, also properly treated to have oxygen 7.0 stoichiometry, show no field-induced effects, in agreement with data reported by Valldor [13], but rather show only linear $M(H)$ from 0 to 9 T in the range $2\,K < T < 70\,K$. We take this behavior to imply that the Yb^{3+} moment is responsible for the field-induced behavior seen in the case of Yb-114.

A potential candidate for the field-induced state is the appearance of a ferromagnetic component arising from, for instance, spin canting of the underlying antiferromagnet state [1]. The high-M state may also represent a transition to a spin-flop state of the antiferromagnet or accompany a field-induced structural transition. Data collected upon field cooling and measuring in fields as low as 50 Oe shows the transition at $T \sim 80\,K$ into the high-magnetization state occurs with substantial temperature hysteresis (H. Claus, pers. comm.) The first-order nature of this transition—both in T and H—makes the canting scenario unlikely and suggests the potential role of a field-induced structural transition.

Definitive interpretation of the in-field behavior from magnetization data alone is difficult because of the unknown role of the rare-earth magnetic moment, its possible ordering, and/or its potential coupling to the Co spin subsystem. We note that a study of $YBaCo_4O_7$ by Valldor [13] does show an irreversibility between ZFC and FC measurements and a presumed ferromagnetic state, but no behavior like that shown in the present case. This again argues that the present phenomenon derives from the magnetic moment of the rare-earth ion. A detailed magnetic and neutron diffraction study on this and the

Fig. 2. (a) Magnetization as a function of temperature measured on warming in 1 T. ZFC = zero-field cooled; FC = field cooled. Inset: Detail of the temperture region near the structural phase transition. (b) Isothermal magnetization measured at 25 K. The arrow marks H_c, the onset of the irreversible field-induced transition. Inset: Hc as function of T. In each case, the sample was ZFC to the measuring temperature from 150 K then the field was applied.

Y-114 analog is presently underway to characterize this field-induced ferromagnetic state.

To understand the structural and magnetic ordering behavior in ZF, a temperature-dependent neutron and synchrotron X-ray powder diffraction study was undertaken. We consider first the high-temperature structure, establishing that present structural models in the literature are incorrect and must be revised. We then address the structural phase transition occurring at 175 K, identifying the driving force behind this transformation, and finally present a preliminary account of the low-temperature antiferromagnetic state.

Neutron powder diffraction data were used to solve the structure of Yb-114 at 225 K. The data were fit to a model with $P31c$ symmetry rather than the $P6_3mc$ symmetry proposed by Rabbow and Mueller-Buschbaum [15] for $LuBaZn_3AlO_7$ and adopted by Valldor and Andersson [14] for R-114 compounds. The distinction is subtle, yet the refinements are compelling. Attempts to refine the neutron data in $P6_3mc$ yield poor calculation of the reflections at high-Q and unsatisfactory refinement statistics ($R(F^2)$ = 13.3% in backscattering bank). In this model, three atoms (Co(2), O(1) and O(2)) lying on a mirror plane show anomalously large thermal parameters, in agreement with what has been reported by Valldor and Andersson [14]. A difference Fourier map of the neutron data clearly indicates that the nuclear density is split equally on either side of the mirror plane, suggesting a lower symmetry. Within the set of space groups with identical extinction conditions to those of $P6_3mc$, $P31c$ is uniquely consistent with the data. In this model the positions of Co(2), O(1) and O(2), not constrained by mirror symmetry, are general and have the same multiplicity (six) as for the $P6_3mc$ model. The refinement of the neutron data in this space group is considerably better ($R(F^2)$ = 5.5% in backscattering bank), with thermal parameters in agreement with what may be expected for this kind of structure. To further improve the model, powder neutron and synchrotron X-ray data collected at 225 K were jointly refined. Fig. 3(a) shows the results of this joint refinement, and details of the structural refinement and derived parameters can be found in Table 1. Bond lengths and angles are reported in Table 2a and b. In particular, we note that the two symmetry independent Co(2)–Co(2) contacts in the Kagomé sheets generate equilateral triangles of two rather different edge lengths, 3.05 and 3.22 Å. A similar pattern of two different size triangles is found in the highly frustrated SCGO, although the difference is somewhat less (2.87 and 2.92 Å) [5]. We note, however, that the Yb-114 structure is more three dimensional than that of SCGO, since in Yb-114 the Ga sites of SCGO are replaced by Co(1) ions with contacts of 3.139 and 3.1855 Å to the Co(2) ions in the plane. That is, a description of Y-114 as a 3-D frustrated lattice (cf. pyrochlore) may be more appropriate (see Fig. 1b).

Despite the different space group assignment, the description of the crystal structure at 225 K based on our
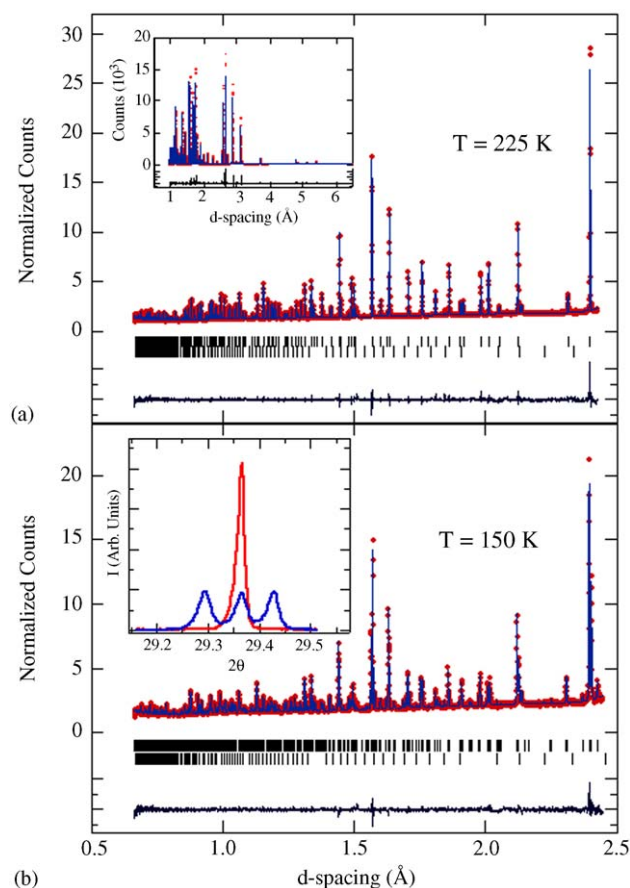

Fig. 3. Neutron diffraction data collected above (a) and below (b) the structural phase transition. In the top curve of each panel, points are experimental data, and the solid line is fit of joint neutron and X-ray refinement of the models in Table 1. The series of vertical lines marks Bragg reflection positions for the main phase (top row) and for the small Yb_2O_3 impurity phase (bottom row, <0.5% by weight). The bottom curve is the difference between calculated and observed data. Insets: (a) X-ray data refinement at 225 K and (b) portion of synchrotron X-ray data collected at 225 and 150 K.

refinement is qualitatively consistent with that presented by Valldor [12]. There are two symmetry-independent CoO_4 tetrahedra in the structure: Co(2) forming the Kagomé sheets and Co(1) linking these sheets along the c-axis. These tetrahedra appear in a 1:3 ratio, suggesting that the formal oxidation state of Co(1) should be 3+ and that of Co(2) should be 2+ in accord with the stoichiometry $YbBaCo^{3+}Co_3^{2+}O_7$. An analogous charge ordering has been proposed for the spinel AlV_2O_8 below 700 K [18]. However, we find that the average Co–O bond lengths in the two tetrahedra are rather similar, $d_{Co(1)-O} = 1.959(3)$ Å and $d_{Co(2)-O} = 1.918(3)$ Å. Tetrahedral coordination of Co^{3+} is extremely rare due to the large crystal field stabilization energy afforded by octahedral coordination. The Co–O bond length in such compounds, 1.79 Å, is typically much shorter than those observed here [19]. This argues against a preferential charge ordering in the Yb-114 compound at 225 K. Indeed, a bond-valence analysis can be performed to estimate the relative fraction of Co^{2+} and

Table 1
Refinement of neutron and X-ray data for YbBaCo$_4$O$_{6.95}$ and YbBaCo$_4$O$_{7.2}$

	YbBaCo$_4$O$_{6.95}$		YbBaCo$_4$O$_{7.2}$ majority phase			YbBaCo$_4$O$_{7.2}$ minority phase		
	225 K	150 K	300 K	100 K	10 K	300 K	100 K	10 K
Space group	P3$1c$	Pbn2$_1$	P3$1c$	Pbn2$_1$	Pbn2$_1$	P3$1c$	P3$1c$	P3$1c$
a (Å)	6.26539(1)	6.25114(1)	6.27023(1)	6.25098(2)	6.253(1)	6.24598(3)	6.23884(3)	6.239(1)
b (Å)		10.89335(2)		10.88658(3)	10.888(2)			
c (Å)	10.22812(2)	10.18697(2)	10.23532(2)	10.18211(3)	10.179(2)	10.23702(8)	10.19473(11)	10.192(3)
V (Å^3)	347.714(1)	693.690(3)	348.496(1)	692.911(4)	693.07(46)	345.863(3)	343.648(4)	343.60(21)
Yb								
x	2/3	0.0034(3)	2/3	0.0015(4)		2/3	2/3	
y	1/3	0.6687(1)	1/3	0.6680(1)		1/3	1/3	
z	0.8766(1)	0.8731(1)	0.87526(9)	0.8725(1)		0.8737(3)	0.8953(10)	
B	1.18(3)	1.14(2)	0.76(2)	0.96(2)		1.43(8)	3.35(13)	
Ba								
x	2/3	0	2/3	0		2/3	2/3	
y	1/3	2/3	1/3	2/3		1/3	1/3	
z	0.5	0.5	0.5	0.5		0.5	0.5230(11)	
B	1.78(3)	1.66(3)	1.63(3)	1.74(3)		1.66(11)	0.52(9)	
Co(1)								
x	0	−0.0107(7)	0	−0.0081(11)		0	0	
y	0	−0.0022(5)	0	−0.0062(5)		0	0	
z	0.4387(4)	0.9393(4)	0.4389(4)	0.9373(4)		0.4349(16)	0.4816(17)	
B	1.47(7)	1.08(6)	1.37(5)	1.03(5)		2.50(15)	1.48(24)	
Co(2)								
x	0.1575(4)		0.1593(5)			0.1736(31)	0.147(5)	
y	0.8150(4)		0.8176(5)			0.8318(31)	0.811(5)	
z	0.6859(3)		0.68551(31)			0.6865(12)	0.7075(19)	
B	1.03(4)		0.92(3)			2.1(1)	1.86(9)	
Co(21)								
x		−0.0097(8)		−0.0021(10)				
y		0.1731(2)		0.1747(2)				
z		0.6878(4)		0.6851(5)				
B		0.82(6)		0.70(6)				
Co(22)								
x		0.2583(7)		0.2577(7)				
y		0.0865(4)		0.0876(4)				
z		0.1875(5)		0.1867(6)				
B		0.36(9)		0.58(12)				
Co(23)								
x		0.2568(7)		0.2548(8)				
y		0.9165(5)		0.9202(4)				
z		0.6833(5)		0.6822(7)				
B		1.19(9)		0.66(16)				
O(1)								
x	0.5149(5)	0.009(2)	0.4880(30)	0.021(4)		0.510(11)	0.467(17)	
y	0.5134(5)	0.0025(5)	0.4917(30)	0.0012(15)		0.524(11)	0.528(17)	
z	0.7489(4)	0.2478(5)	0.7506(6)	0.2419(9)		0.7425(26)	0.7349(29)	
B	2.05(6)	0.38(9)	3.68(16)	2.38(12)		2.76(32)	3.79(55)	
O(2)								
x	0		0			0	0	
y	0		0			0	0	
z	0.2444(5)		0.2410(10)			0.233(4)	0.116(5)	
B	1.10(3)		3.68(16)			2.76(32)	3.79(55)	
O(22)								
x		0.0114(22)		0.012(4)				
y		0.4919(5)		0.4824(11)				
z		0.2465(7)		0.2454(13)				
B		1.55(9)		2.38(12)				

Table 1 (*continued*)

	YbBaCo$_4$O$_{6.95}$		YbBaCo$_4$O$_{7.2}$ majority phase			YbBaCo$_4$O$_{7.2}$ minority phase		
	225 K	150 K	300 K	100 K	10 K	300 K	100 K	10 K
O(22′)								
x		0.7731(13)		0.7811(21)				
y		0.2552(6)		0.2614(15)				
z		0.7761(9)		0.7672(15)				
B		1.2(2)		2.38(12)				
O(23)								
x		0.7205(12)		0.6859(23)				
y		0.7504(6)		0.7452(14)				
z		0.2201(9)		0.2365(15)				
B		1.3(2)		2.38(12)				
O(3)								
x	0.1157(4)		0.1240(13)			0.159(11)	0.079(5)	
y	0.7810(4)		0.7937(13)			0.840(11)	0.769(4)	
z	0.5005(3)		0.5008(6)			0.4907(23)	0.4920(33)	
B	1.58(2)		3.68(16)			2.76(32)	3.79(55)	
O(31)								
x		−0.0445(8)		−0.0366(23)				
y		0.1631(6)		0.1397(11)				
z		0.5015(8)		0.5023(15)				
B		1.8(1)		2.38(12)				
O(32)								
x		0.2294(10)		0.2442(25)				
y		0.1014(5)		0.0993(16)				
z		−0.0047(11)		−0.0171(18)				
B		1.04(9)		2.38(12)				
O(33)								
x		0.2694(11)		0.2479(29)				
y		0.9350(5)		0.9238(16)				
z		0.4977(12)		0.5056(19)				
B		1.73(9)		2.38(12)				
R_{wp}	6.35	6.08	9.36	10.67	12.45			
χ^2	4.62	3.89	6.34	5.45	8.63			

Co^{3+} on the two distinct sites. This analysis involves minimizing the function (1) [20]:

$$T = \sum_{i=1,2} n_i \sum_{j=2,3} (B_{ij} - j)^2 \qquad (1)$$

subject to the constraints of stoichiometry and full occupancy of each site [21]. In (1), n_i is the number of symmetry related sites i (i.e., $i = 1$ for Co(1) and 3 for Co(2)), j labels the possible valence states of Co, and B_{ij} is the calculated bond valence sum (BVS) for site i assuming it is occupied by a Co ion of charge j. A random distribution would assign to each site 75% Co^{2+} and 25% Co^{3+}. Applied to the 225 K structural model, we find that Co(1) is 89.9% Co^{2+} and 10.1% Co^{3+}, while Co(2) site is 70.0% Co^{2+} and 30.0% Co^{3+}. This calculation suggests a slight preference for Co^{2+} on the linking Co(1) site, the opposite of what would be predicted for the charge-ordered model.

However, inspection of the d_{Ba-O} shown in Table 2a reveals that Ba^{2+} is severely underbonded, pointing to a structural instability. There are only three Ba–O contacts less than 3 Å (2.809 Å); the remaining nine contacts are (three of each) 3.119, 3.147 and 3.456 Å, which cannot realistically be classified as Ba–O bonds. An average d_{Ba-O} of 3.13 Å and a computed BVS of 1.33 demonstrate convincingly that the O environment does not satisfy the bonding requirements of the large Ba^{2+} ion [22].

To compensate for this underbonding, Yb-114 undergoes a structural phase transition at 175 K. Fig. 3(b) shows the results of a joint Rietveld refinement of neutron and X-ray data collected at 150 K, while the inset shows a portion of the synchrotron X-ray data, collected at both 225 K (above) and 150 K (below the transition). The splitting of the reflection into three peaks, as seen in the inset data, indicates that the low-temperature phase has orthorhombic or lower symmetry. Indeed, both X-ray and neutron data can be indexed and refined on a doubled supercell with dimensions $1 \times \sqrt{3} \times 1$ with respect to the $P31c$ high-temperature phase. The major component of the structural distortion involves a peak splitting scheme

Table 2

225 K		150 K	
(a) Atomic distances for YbBaCo₄O₆.₉₅			
Yb–O(1)	2.227(3)	Yb–O(22)	2.176(6)
Yb–O(3)	2.226(3)	Yb–O(22′)	2.203(6)
		Yb–O(23)	2.247(7)
		Yb–O(31)	2.266(7)
		Yb–O(32)	2.209(9)
		Yb–O(33)	2.241(7)
Ba–O(1)	3.120(4)		
	3.147(4)		
		Ba–O(22)	3.147(4)
			3.147(4)
		Ba–O(22′)	2.818(10)
			3.428(10)
		Ba–O(23)	2.782(10)
			3.467(10)
Ba–O(3)	2.809(2)	Ba–O31	2.848(5)
	3.456(2)		3.404(5)
		Ba–O32(O33)	2.906(6)
			3.374(6)
Co(1)–O(1)		Co(1)–O(1)	1.951(5)
Co(1)–O(2)	1.987(5)	Co(1)–O(22)	3.577(14)
		Co(1)–O(22′)	3.528(9)
		Co(1)–O(23)	3.794(9)
Co(1)–O(3)	1.950(3)	Co(1)—O(31)	1.895(9)
		Co(1)–O(32)	1.963(8)
		Co(1)–O(33)	1.872(9)
Co(1)–Co(2)	3.139(3)	Co(1)–Co(21)	3.145(5)
	3.185(3)		3.195(5)
		Co(1)–Co(22)	3.134(6)
			3.187(6)
		Co(1)–Co(23)	3.068(6)
			3.223(6)
Co(2)–O(1)	1.903(4)	Co(21)–O(1)	2.008(6)
		Co(21)–O(22′)	1.858(9)
		Co(21)–O(23)	2.017(8)
		Co(21)–O(31)	1.914(9)
Co(2)–O(2)	1.954(2)	Co(22)–O(1)	1.911(13)
		Co(22)–O(22′)	1.948(9)
		Co(22)–O(22)	1.870(12)
		Co(22)–O(32)	1.973(12)
Co(2)–O(3)	1.912(4)	Co(23)–O(1)	1.991(13)
		Co(23)–O(22)	1.985(12)
		Co(23)–O(23)	1.871(8)
		Co(23)–O(33)	1.903(13)
Co(2)–Co(2)	3.051(2)	Co(22)–Co(21)	2.994(6)
	3.222(2)		3.227(5)
		Co(22)–Co(23)	3.032(3)
			3.221(3)
(b) Bond angles for YbBaCo₄O₆.₉₅			
O(1)–Yb–O(1)	89.07(15)	O(22)–Yb–O(32)	95.70(34)
O(1)–Yb–O(3)	94.47(10)	O(32)–Yb–O(23)	93.69(31)
	85.97(10)	O(23)–Yb–O(31)	90.84(27)
	173.87(8)	O(31)–Yb–O(22′)	90.10(26)
		O(22′)–Yb–O(33)	87.59(31)
O(3)–Yb–O(3)	90.78(11)	O(33)–Yb–O(22)	84.4(4)
O(3)–Ba–O(3)	120.00(0)	O(31)–Ba–O(32)	61.21(17)
		O(32)–Ba–O(22″)	88.43(22)
		O(22′)–Ba–O(23)	107.75(16)
		O(23)–Ba–O(22)	62.09(22)
		O(23)–Ba–O(31)	119.71(21)
O(3)–Co(1)–O(3)	110.02(12)	O(1)–Co(1)–O(31)	109.3(4)
O(3)–Co(1)–O(2)	108.92(13)	O(1)–Co(1)–O(32)	106.6(5)
		O(1)–Co(1)–O(33)	108.9(6)

Table 2 (*continued*)

225 K		150 K	
		O(33)–Co(1)–O(31)	114.4(4)
		O(33)–Co(1)–O(32)	110.1(4)
		O(31)–Co(1)–O(32)	107.2(3)
O(1)–Co(2)–O(1)	111.70(22)	O(1)–Co(21)–O(22′)	108.3(4)
O(1)–Co(2)–O(2)	104.23(15)	O(1)–Co(21)–O(23)	109.9(5)
	113.28(15)	O(1)–Co(21)–O(31)	104.4(3)
O(2)–Co(2)–O(3)	106.78(16)	O(22′)–Co(21)–O(23)	112.1(5)
O(1)–Co(20–O(3)	116.75(16)	O(22′)–Co(21)–O(31)	115.1(4)
	104.27(16)	O(23)–Co(21)–O(31)	106.7(4)
		O(1)–Co(22)–O(22)	105.2(4)
		O(1)–Co(22)–O(22′)	108.3(4)
		O(1)–Co(22)–O(32)	106.5(3)
		O(22)–Co(22)–O(22′)	107.6(4)
		O(22)–Co(22)–O(32)	115.8(4)
		O(22′)–Co(22)–O(32)	113.0(4)
		O(1)–Co(23)–O(22)	109.8(4)
		O(1)–Co(23)–O(23)	105.3(4)
		O(1)–Co(23)–O(33)	108.4(3)
		O(22)–Co(23)–O(23)	121.4(4)
		O(23)–Co(23)–O(33)	103.6(4)
		O(33)–Co(23)–O(1)	107.9(4)
Co(2)–O(1)–Yb	122.17(13)	Co(1)–O(1)–Co(21)	107.6(4)
	131.24(14)	Co(1)–O(1)–Co(22)	108.5(5)
		Co(1)–O(1)–Co(23)	109.7(6)
Co(2)–O(1)–Co(2)	106.56(16)	Co(21)–O(1)–Co(22)	110.8(5)
		Co(21)–O(1)–Co(23)	108.9(5)
		Co(22)–O(1)–Co(23)	111.24(27)
Co(1)–O(2)–Co(2)	107.84(13)	Yb–O(22)–Ba	91.8(2)
Co(2)–O(2)–Co(2)	111.05(12)	Yb–O(22)–Co(23)	131.8(7)
		Yb–O(22)–Co(23)	124.2(6)
		Ba–O(22)–Co(22)	93.7(3)
		Ba–O(22)–Co(23)	89.9(4)
		Co(22)–O(22)–Co(23)	103.7(3)
		Yb–O(22′)–Ba	99.3(3)
		Yb–O(22′)–Co(21)	125.7(3)
		Yb–O(22′)–Co(22)	123.3(4)
		Ba–O(22′)–Co(21)	99.7(4)
		Ba–O(22′)–C(22)	97.6(3)
		Co(21)–O(22′)–Co(22)	103.7(4)
		Yb–O(23)–Ba	97.6(3)
		Yb–O(23)–Co(21)	119.5(4)
		Yb–O(23)–Co(23)	126.4(4)
		Ba–O(23)–Co(21)	100.3(4)
		Ba–O(23)–Co(23)	102.4(4)
		Co(21)–O(23)–Co(23)	105.1(3)
Yb–O(3)–Ba	98.42(8)	Yb–O(31)–Ba	95.7(2)
Yb–O(3)–Co(1)	123.00(16)	Yb–O(31)–Co(1)	122.3(4)
Yb–O(3)–Co(2)	121.96(16)	Yb–O(31)–Co(21)	120.9(3)
Ba–O(3)–Co(1)	99.37(9)	Ba–O(31)–Co(1)	101.1(3)
Ba–O(3)–Co(2)	97.24(12)	Ba–O(31)–Co(21)	96.8(3)
Co(1)–O(3)–Co(2)	108.74(18)	Co(1)–O(31)–Co(21)	111.3(4)
		Yb–O(32)–Ba	95.4(2)
		Yb–O(32)–Co(1)	127.3(5)
		Yb–O(32)–Co(22)	121.2(4)
		Ba–O(32)–Co(1)	97.3(3)
		Ba–O(32)–Co(22)	95.8(3)
		Co(1)–O(32)–Co(22)	108.1(4)
		Yb–O(33)–Ba	96.8(3)
		Yb–O(33)–Co(1)	125.5(6)
		Yb–O(32)–Co(23)	122.4(4)
		Ba–O(33)–Co(1)	95.3(3)
		Ba–O(33)–Co(23)	96.0(4)
		Co(1)–O(33)–Co(23)	108.7(4)

consistent with a C-centered orthorhombic cell (space group $Cmc2_1$). However, a number of extremely weak reflections that violate C-centering extinction conditions are observed in the X-ray data and more clearly in the neutron data, indicating that the true symmetry is primitive with space group $Pbn2_1$. The higher sensitivity of neutrons to light O atom displacements indicates that these are primarily responsible for the weak superlattice peaks with primitive indexing. In this space group, there are no special positions and all atoms occupy sites of multiplicity four. Full structural refinement data and derived parameters are reported in Tables 1 and 2.

Crucially, our refinements provide no compelling structural evidence for charge ordering of Co^{2+}/Co^{3+} as a mechanism for the transition. In the low-temperature structure there are four distinct Co sites: one deriving from Co(1) in the high-temperature phase, and three deriving from Co(2). In this case, a similar BVS analysis to that used for the high-temperature structure yields % Co^{2+} of 69.5, 81.6, 72.0, and 77.0 for Co(1), Co(21), Co(22), and Co(23), respectively. While some values have changed from those found at 225 K, they are all very close to those expected for a random Co^{2+}/Co^{3+} distribution. It is difficult to argue that a charge ordering has occurred on cooling through this phase transition.

On the other hand Fig. 4 makes clear that the Ba–O coordination polyhedron has drastically transformed from its high-temperature configuration. Although the average $d_{Ba–O}$ has not changed from its value of 3.13 Å above the transition, several Ba–O contacts have shortened considerably due to this distortion. Indeed, there are now six contacts $\leqslant 3.05$ Å, compared to only three at 225 K, and the BVS has increased to 1.54. In the process of enhancing the Ba–O bonding environment, the Co(2)O$_4$ tetrahedra have rotated cooperatively to buckle the Kagomé plane and remove its three-fold symmetry. In response, the
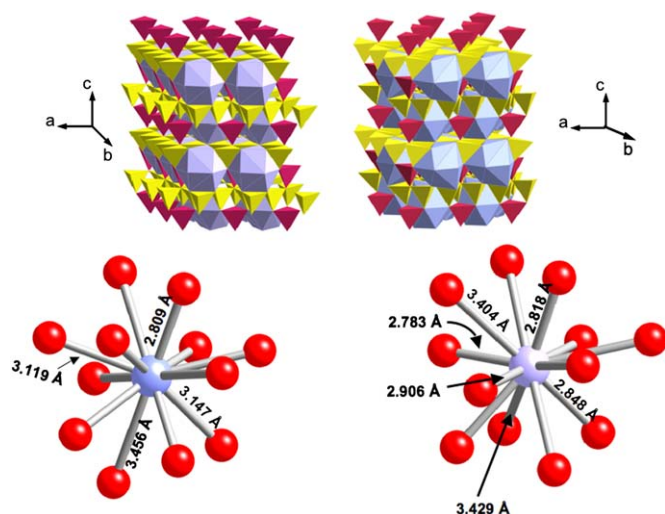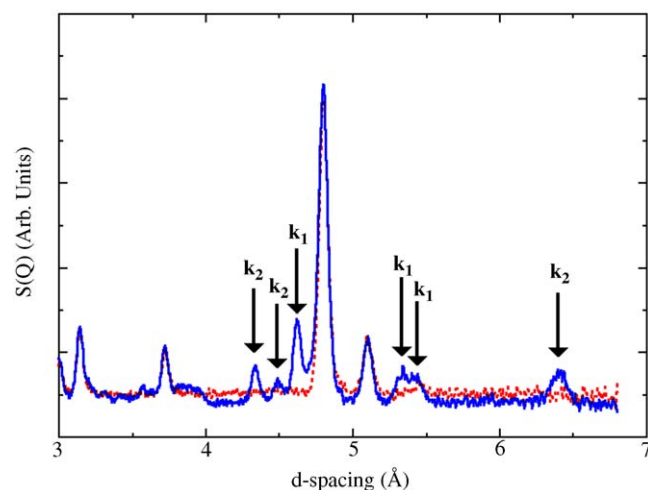

Fig. 5. Portion of neutron diffraction data collected on the GEM diffractometer at 90 K (dashed) and 1.7 K (solid). Magnetic scattering due to antiferromagnetic order in the 1.7 K pattern is marked by the two observed propagation vectors, $\mathbf{k}_1 = (0,0,0)$ and $\mathbf{k}_2 = (1/2,0,0)$.

Co–Co contacts in the distorted Kagomé plane are now unequal, as shown in Table 2.

These unequal Co–Co contacts imply a breaking of the geometric frustration present in the high temperature, trigonal phase in accord with a transition to long-range AFM order below 80 K. As shown in the neutron diffraction data of Fig. 5, antiferromagnetic reflections present below 80 K can be indexed on two propagation vectors of the $Pbn2_1$ space group, $\mathbf{k}_1 = (0,0,0)$ and $\mathbf{k}_2 = (1/2,0,0)$. However, the data collected on the HRPD instrument do not provide adequate Q-range and statistics to allow a complete solution of the magnetic structure. We are in the process of collecting full, temperature-dependent data to solve completely the magnetic structure of Yb-114. We do note, however, that preliminary data we have collected on the YBaCo$_4$O$_7$ analog show only reflections belonging to the $\mathbf{k}_1 = (0,0,0)$ propagation vector (L. Chapon, pers. comm.). It is thus reasonable to conclude that the $\mathbf{k}_2$ component involves a contribution from the rare earth.

Finally, we return to the issue of the biphasic sample, YbBaCo$_4$O$_{7.2}$. Fig. 6 compares synchrotron data for the single-phase and biphasic samples. The degenerate (3,1,3) and (3,1,−3) reflection of the two phases at 225 K is marked, as are the split peaks (indexed as (3,5,3), (4,2,3) with three overlapped reflections (2,7,1), (2,3,6), (1,7,3)) at 150 K. We have been able to refine separately the lattice constants of both phases at 300 and at 100 K, which are reported in Table 1. The minority phase clearly has a different unit cell. The lattice constants of the majority phase are extremely close to those of the single-phase Yb-114 sample, indicating that this majority component of the biphasic sample is very close to stoichiometric. We thus suggest that the excess O is essentially entirely in the minority component, the two phases being separated by a
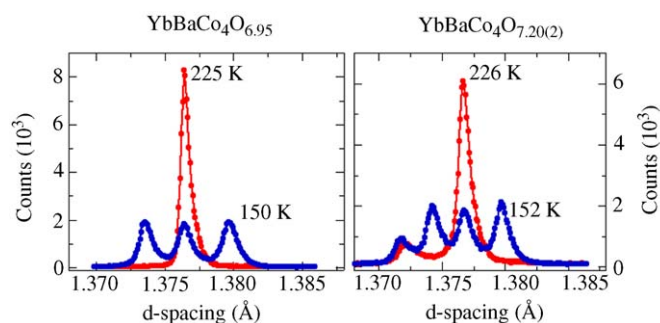

Fig. 4. Crystal structure of YbBaCo$_4$O$_7$ at 225 K (left) and 150 K (right) based on joint refinement of neutron and X-ray powder data. Coordination of O to the Ba site is highlighted in the bottom half of the figure.

Fig. 6. Comparison of synchrotron X-ray powder diffraction collected above and below the crystallographic phase transition in the single-phase $YbBaCo_4O_{6.95}$ and biphasic $YbBaCo_4O_{7.2}$ samples. The arrow points to the scattering from the minority phase that does not transform upon cooling (see text).

miscibility gap. As Valldor and Andersson [14] have pointed out, it is difficult to speculate where this excess O can go in the rather densely packed crystal structure. It is possible that the 'excess' oxygen in fact reflects a cation deficiency, in much the same way as $LaMnO_{3+\delta}$ [23]. Diffraction experiments on pure $RBaCo_4O_{8.5}$ samples to identify the potential location of excess O or the presence of metal-ion deficiency are in progress.

In Fig. 6 it is noteworthy that only the majority component undergoes the phase transformation; X-ray data show that the minority phase remains in the $P31c$ group down to 10 K. Assuming that interstitial O can be accommodated, we can speculate that the excess O may enhance the Ba–O bonding to the extent that the $P31c \rightarrow Pbn2_1$ transformation is no longer favorable. One intriguing possibility is that the O-rich phase, remaining in the high symmetry structure, will not order antiferromagnetically but rather will be magnetically frustrated.

In summary, we have studied the magnetic and structural properties of the Yb-114 system. At room temperature, the system is geometrically frustrated, with a 3-D structural motif related to that of the pyrochlore lattice. A long-range antiferromagnetic state develops below 80 K after the three-fold degeneracy of the structure is lifted by a trigonal→orthorhombic phase transition at 175 K. We have identified that this phase transition is driven by a drastically underbonded Ba^{2+} ion seeking to satisfy its bond valence requirements. It is not unreasonable to assume that this instability may be found in other members of the R-114 family as well, suggesting a re-evaluation of the structures and their temperature dependence. The pure, zero-field-cooled AFM state in Yb-114 is unstable to moderate magnetic fields, irreversibly developing a magnetic moment above a threshold field. We find that specimens with excess oxygen form biphasic mixtures of isostructural phases, but that the oxygen hyperstoichiometric component does not undergo the crystallographic phase transition. Studies are underway to isolate a pure phase sample of this oxygen-rich material and to establish

whether such an undistorted structure will express its geometric frustration in the spin sector.

Appendix A. Supplementary materials

Supplementary data associated with this article can be found in the online version at doi:10.1016/j.jssc.2006.01.010.

References

[1] R. Ballou, B. Canals, M. Elhajal, C. Lacroix, A.S. Wills, Phys. Stat. Sol. 236 (2003) 240–245.
[2] J. Greedan, J. Mater. Chem. 11 (2001) 37–53.
[3] A. Harrison, J. Phys.: Condens. Matter 16 (2004) S553–S572.
[4] C. Broholm, G. Aeppli, S.-H. Lee, W. Bao, J.F. DiTusa, J. Appl. Phys. 79 (1996) 5023–5028.
[5] S.-H. Lee, C. Broholm, G. Aeppli, T.G. Perring, B. Hessen, A. Taylor, Phys. Rev. Lett. 76 (1996) 4424–4427.
[6] X. Obradors, A. Labarta, A. Isalgue, J. Tejada, J. Rodriguez, M. Pernet, Solid State. Commun. 65 (1988) 189–192.
[7] P. Schiffer, A.P. Ramirez, Comments Condens. Matter Phys. 18 (1996) 21–50.
[8] P. Schiffer, A.P. Ramirez, K.N. Franklin, S.-W. Cheong, Phys. Rev. Lett. 77 (1996) 2085–2088.
[9] G.L. Bychkov, S.N. Barilo, S.V. Shiryaev, D.V. Sheptyakov, S.N. Ustinovich, A. Podlesnyak, M. Baran, R. Szymczak, A. Furrer, J. Cryst. Growth 275 (2005) e813–e818.
[10] E.V. Tsipis, D.D. Khalyavin, S.V. Shiryaev, K.S. Redkina, P. Nunez, Mater. Chem. Phys. 92 (2005).
[11] E.V. Tsipis, V.V. Kharon, J.R. Frade, P. Nunez, J. Solid State. Electrochem. 9 (2005) 547–557.
[12] M. Valldor, Solid State Sci. 6 (2004) 251–266.
[13] M. Valldor, J. Phys.: Condens. Matter 16 (2004) 9209–9225.
[14] M. Valldor, M. Andersson, Solid State Sci. 4 (2002) 923–931.
[15] C. Rabbow, H. Mueller-Buschbaum, Z. Naturforsch. 51b (1996) 343–347.
[16] J. Rodriguez-Carvajal, FULLPROF: A Program for Rietveld Refinement and Pattern Matching Analysis, in: Proceedings of the Satellite Meeting on Powder Diffraction of the XV Congress of the IUCr, Toulouse, France, 1990, p. 127.
[17] A.C. Larson, R.B. Von Dreele, General Structure Analysis System (GSAS) Los Alamos National Laboratory Report LAUR 86-748, 2000.
[18] K. Matsuno, T. Katufuji, S. Mori, Y. Moritomo, A. Machida, E. Nishibori, M. Takata, M. Sakata, N. Yamamoto, H. Takagi, J. Phys. Soc. Jpn. 70 (2001) 1456–1459.

[19] G. Muncaster, G. Sankar, C.R.A. Catlow, J.M. Thomas, S.J. Coles, M. Hursthouse, Chem. Mater. 12 (2000) 16.

[20] S.E. Wright, J.A. Foley, J.M. Hughes, Am. Miner. 85 (2000) 524–531.

[21] Bond valence sum parameters for M–O bonds: four-coordinate Co^{2+}: $d_0 = 1.704$ Å (see Wood et al. Inorg. Chem. 37, (1998) 4149); four-coordinate Co^{3+}: $d_0 = 1.673$ Å (see reference [19]); Ba^{2+}: $d_0 = 2.285$ Å. In all cases, $b = 0.37$ Å.

[22] This high degree of underbonding argues against stabilizing this structure with smaller divalent cations on the Ba^{2+} site.

[23] J.A.M. van Roosmalen, P. van Vlaanderen, E.H.P. Cordfunke, W.L. Ijdo, D.J.W. Ijdo, J. Solid State Chem. 114 (1995) 516–523.